J Mater Sci (2014) 49:2496–2508
DOI 10.1007/s10853-013-7945-x

Mechanical characterization of hollow ceramic nanolattices

Lucas R. Meza · Julia R. Greer

Received: 28 September 2013 / Accepted: 2 December 2013 / Published online: 18 December 2013

Abstract In the analysis of complex, hierarchical structural meta-materials, it is critical to understand the mechanical behavior at each level of hierarchy in order to understand the bulk material response. We report the fabrication and mechanical deformation of hierarchical hollow tube lattice structures with features ranging from 10 nm to 100 μm, hereby referred to as nanolattices. Titanium nitride (TiN) nanolattices were fabricated using a combination of two-photon lithography, direct laser writing, and atomic layer deposition. The structure was composed of a series of tessellated regular octahedra attached at their vertices. In situ uniaxial compression experiments performed in combination with finite element analysis on individual unit cells revealed that the TiN was able to withstand tensile stresses of 1.75 GPa under monotonic loading and of up to 1.7 GPa under cyclic loading without failure. During the compression of the unit cell, the beams bifurcated via lateral-torsional buckling, which gave rise to a hyperelastic behavior in the load–displacement data. During the compression of the full nanolattice, the structure collapsed catastrophically at a high strength and modulus that agreed well with classical cellular solid scaling laws given the low relative density of 1.36 %. We discuss the compressive behavior and mechanical analysis of the unit cell of these hollow TiN nanolattices in the context of finite element analysis in combination with classical buckling laws, and the behavior of the full structure in the context of classical scaling laws of cellular solids coupled with enhanced nanoscale material properties.

L. R. Meza (✉) · J. R. Greer
Division of Engineering and Applied Science, California Institute of Technology, 1200 E California Blvd, Pasadena, CA 91125, USA
e-mail: lmeza@caltech.edu

J. R. Greer
Kavli Nanoscience Institute, California Institute of Technology, 1200 E California Blvd, Pasadena, CA 91125, USA
e-mail: jrgreer@caltech.edu

Introduction

To predict the mechanical behavior of architected materials, it is first necessary to understand the interplay between structural performance and the intrinsic mechanical properties of the constituent material. Periodic three-dimensional (3D) structures with nanoscale constituents, often referred to as "meta-materials," are being extensively investigated, with new materials like carbon nanotube foams [1–3], metallic microlattices [4, 5], and biomimetic composites [6] being actively pursued thanks to advances in nanoscale fabrication and metrology techniques. While such nano-architected meta-materials exhibit novel mechanical properties, of particular interest is the ability to extract the intrinsic properties of constituent materials using simple mechanical tests like tension and compression experiments. Bulk mechanical properties of cellular solids are typically described using the material properties, the geometry, and the relative density ($\bar{\rho} = \rho/\rho_s$) of the structure [7–12]. Material properties are generally assumed to be scale-invariant, which implies that cellular solids with the same geometry and material composition will have the same moduli and strengths regardless of their absolute size. This assumption appears to break down when the dimensions of the structure approach the characteristic length scale of the material microstructure, as is the case in hard biomaterials like nacre and bird beaks, whose properties extend beyond the rule of mixtures [13–15]. A natural

question that emerges is whether the breakdown of the classically derived mechanical behavior is caused by a change in the failure mechanism when nano-sized components are introduced or if it stems from a size effect in the mechanical properties of the constituent material? To describe and predict the overall deformation behavior of nanostructured meta-materials, it is critical to understand both structural and material-induced behavior at each fundamental level of hierarchy.

We report the fabrication and mechanical deformation of hollow ceramic nanolattices comprised of elliptical beams. The characteristic dimensions of these 3D structures range from tens of nanometers (wall thickness) to several microns (tube diameter) to tens of microns (unit cell) to over 100 μm for the entire structure. The relative density of the structure, defined as the volume fraction of material in a single unit cell, was calculated to be $\bar{\rho} = 0.0136$. The constituent solid material is titanium nitride (TiN), which was deposited via atomic layer deposition (ALD). The smallest characteristic length scale is represented by the wall thickness of 75 nm, which is of the same order of magnitude as the grain size in TiN, measured to be 10–20 nm using transmission electron microscopy (TEM) (Fig. 2c). In situ nanomechanical experiments and finite element simulations on the deformation of a single unit cell of the structure revealed a remarkably high von Mises stress of 2.50 GPa and a tensile yield strength, also referred to as the modulus of rupture, of 1.75 GPa within the TiN walls, which corresponds to an elastic limit of 1.8 % using a Young's modulus of 98 GPa. We show that this high tensile strength, coupled with a lateral-torsional buckling instability observed during the uniaxial compression of the unit cell, gave rise to a hyperelastic deformation response. Compression experiments performed on the full nanolattice gave a structural modulus of $E = 61.8$ MPa and yield strength of $\sigma_y = 0.873$ MPa. We postulate that the observed structural response of the nanolattice can be well explained using classical mechanics theories, and that nanoscale size effects in the material properties can explain the enhanced constituent material mechanical properties.

Materials and methods

Fabrication

The nanolattices were constructed using a multi-step negative pattern fabrication process involving direct laser writing (DLW), two-photon lithography (TPL), atomic layer deposition (ALD), and O_2 plasma etching (Fig. 1). A polymer scaffold was first written using the Photonic Professional DLW instrument (Nanoscribe GmbH, Germany), which makes use of a TPL DLW process in a photopolymer to create 3D structures with features as small as 150 nm [16]. This scaffold was conformally coated with 75 nm of TiN using a plasma enhanced ALD process in the Oxford OpAL ALD system (Oxfordshire, UK). The internal polymer was then exposed using focused ion beam (FIB) milling in the FEI Nova 200 NanoLab and dissolved using O_2 gas in a barrel plasma etcher, leaving behind a hollow truss structure. More precise fabrication details can be found in [17].

Structure

The geometry used in these experiments was derived from a series of tessellated regular octahedron unit cells connected at their vertices (as shown in Fig. 2a, b). Each octahedron was composed of 7 μm-long hollow struts with vertically oriented elliptical cross-sections. The resulting structure was a 100-μm cube comprised of a $10 \times 10 \times 10$ array of octahedron unit cells. An octahedron is an inherently rigid geometry, which has no collapse mechanisms [8, 9]. The octahedra in the nanolattices were arranged into a structure with a relatively low connectivity ($Z = 8$) and formed a bending-dominated structure with periodic collapse mechanisms [8].

Experimental setup

The individual unit cells and the full nanolattice structures were quasi-statically compressed to failure in an in situ nanoindentation instrument InSEM (Nanomechanics, Inc., Tenessee) previously referred to as SEMentor (see [18] for a specification of the instrument). Individual unit cells were compressed along their vertical axis (Fig. 3b) at a constant prescribed displacement rate of 10 nm s^{-1}, and the full structure was compressed at 250 nm s^{-1}. Additional cyclic loading experiments were performed on single unit cells in which 11 load–unload cycles were done at the same loading rate as for the individual unit cell to a displacement of 350 nm with a subsequent unloading to 10 % of the maximum load in the cycle. Prior to the tests, the instrument was fully stabilized for at least 12 h to minimize the thermal drift effect. Typical thermal drift rates after such stabilization in this instrument are below 0.05 nm s^{-1}, which implies that displacement due to thermal drift was likely a negligible contribution to the measured displacement.

Careful imaging of the fabricated structures revealed that the truss beams had elliptical cross-sections with a major axis of $a = 600$ nm, a minor axis of $b = 134$ nm, and a thickness $t = 75$ nm. The effective length of the beams was taken to be $L = 6.5$ μm based on the geometry of the unit cell. The modulus of elasticity used was $E = 98$ GPa, which was approximated by matching the stiffness calculated through

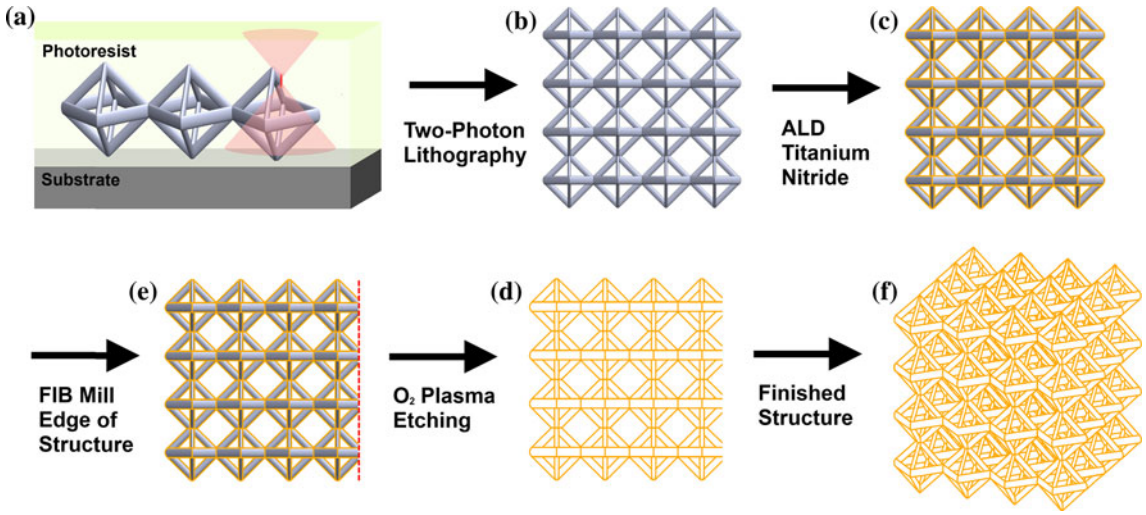

Fig. 1 Nanolattice fabrication process. **a**, **b** Schematic representation of the writing process of the lattice unit cells using two-photon lithography direct laser writing. **c** Structure is coated using an atomic layer deposition (ALD) process. **d** One edge of the sample is milled using a focused ion beam (FIB) to expose the polymer. **e** The internal polymer is etched away using an O_2 plasma. **f** Final product: a hollow tube nanolattice (Color figure online)

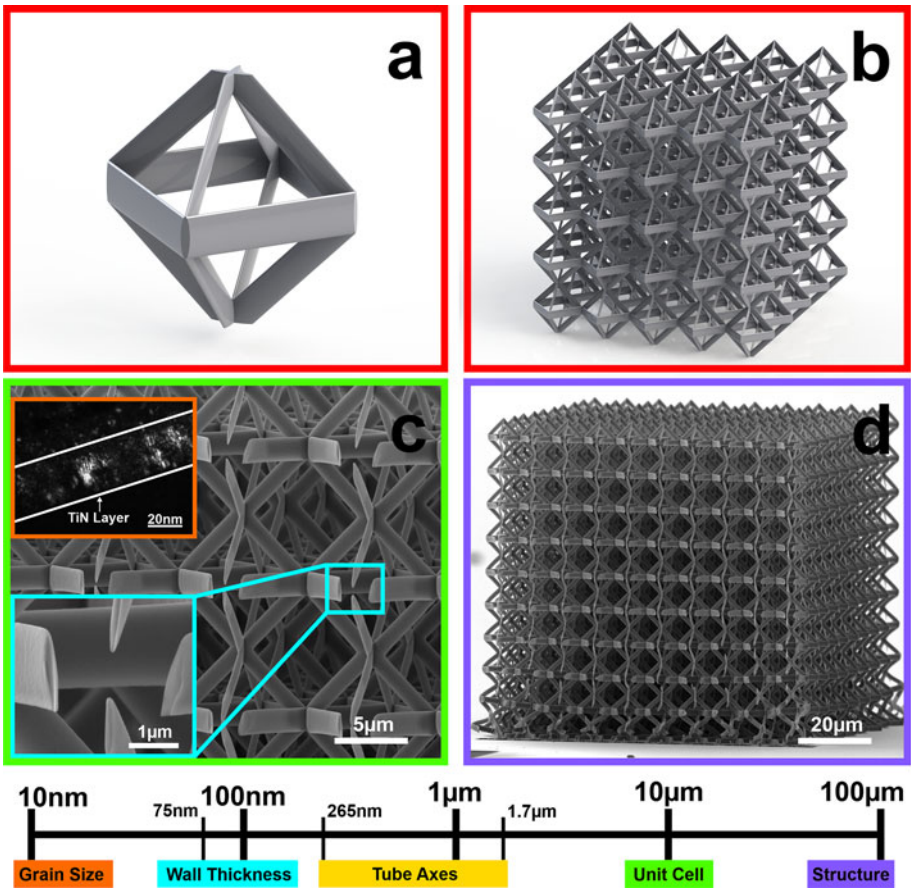

Fig. 2 Nanolattice design and hierarchy. **a** Computer-aided design of an elliptical tube octahedron unit cell. **b** Computer-aided design of the full nanolattice. **c** SEM image of the FIB milled edge of a nanolattice. *Top left inset* shows a dark-field TEM image of the TiN microstructure, which reveals nano-sized grains. *Bottom left inset* a zoomed image of the hollow tubes. **d** SEM image of the full octahedron structure (Color figure online)

the FEM simulations with that of the experiments. When this modulus was taken with a Poison's ratio of $\nu = 0.295$ for titanium nitride, the shear modulus of the beam was calculated as $G = 37.8$ GPa.

Finite element methods

FEM simulations of the uniaxial compression of the top four beams of a single unit cell were performed in the finite

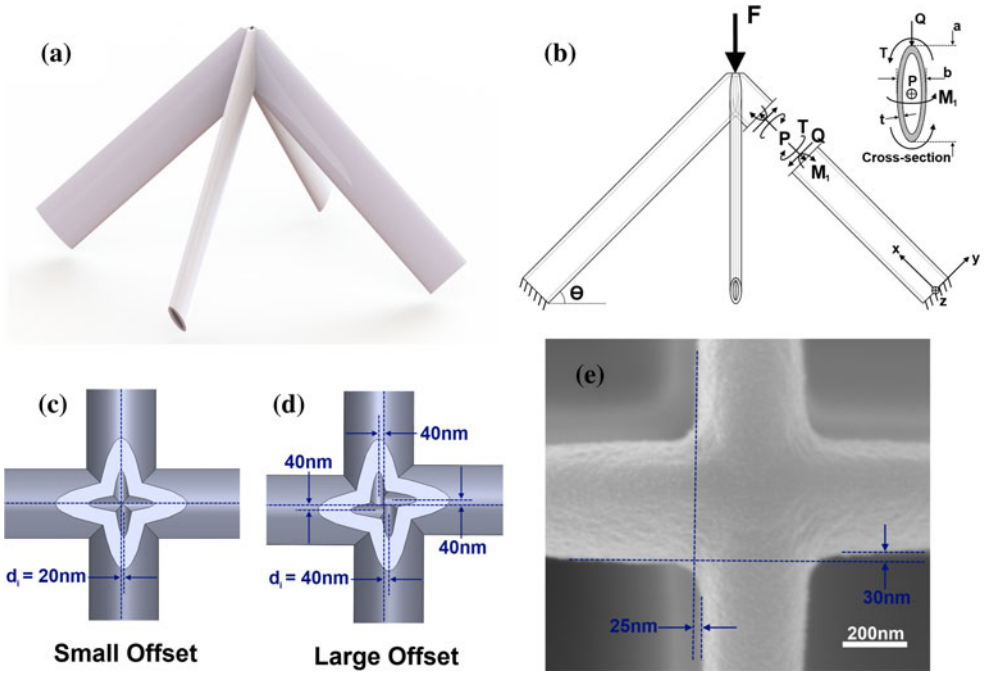

Fig. 3 Unit cell design and simulations. **a** Computer-aided design of the simplified 4-bar structure used in FEM simulations. **b** Diagram showing the force and moment balance on the simplified 4-bar unit cell. **c**, **d** Computer-aided design of 20- and 40-nm offset structures tested in FEM simulations. **e** SEM top view of actual unit cell showing the offset (Color figure online)

element software ABAQUS. A nonlinear elastic geometry solver was implemented in the simulations to account for the significant deflection of the beams. A linear elastic solver would have been sufficient to model the stress and deformation of the beams up to the point of buckling but would have been unable to capture the elastic instability and the large post-buckling deformation. The structure was modeled using the CAD program SolidWorks to obtain a geometry that precisely reflected that of the real structure. A simplified model of the unit cell consisting of only the upper four beams was used in order to better isolate the beam buckling response (Fig. 3a) and to create a better analog to the analytical buckling model. All four beams were modeled to ensure that the resulting behavior was due to structural interactions and not to any imposed symmetry boundary conditions. These four beams met with a small counter-clockwise lateral offset in the central node of the structure, mimicking the geometry of the actual unit cell (Fig. 3e). The degree of the offset plays an important role in the resulting deformation of the structure, a point that is discussed in the following sections.

A rigid boundary condition was applied to the lower end of each of the four beams of the unit cell to simplify the FEM model (Fig. 3b). A stiff elastic boundary condition would most accurately represent the unit cell, but it is difficult to determine the exact stiffness of the lower boundary due to the complex geometry and nodal connectivity. Instead, an FEM model of a full unit cell was made and tested for the sake of validating the simplified model, and the buckling response and stress concentrations were found to be nearly identical, giving validation to both the simplified unit cell and the fixed lower boundary. Only the results of the simplified unit cell are shown here for the sake of isolating the behavior of the beams in buckling.

A displacement boundary condition was applied to the top face of the structure to match the experimental conditions. No lateral constraint was placed on the top face, so the structure was free to translate and rotate about the central node. A tetrahedral mesh was used to accommodate the complex geometry of the unit cell. The mesh was manually refined until the maximum stresses observed in the structure had fully converged at a final average mesh density of 400,000 elements μm^{-3}, with a higher concentration of elements toward the central node of the structure.

Analysis

Loading conditions

To capture the physical foundation for the observed deformation response, it is helpful to define and to quantify the resultant forces and moments acting on individual beams. We consider the same four beam structure with identical boundary conditions to those used in the FEM simulations. The only external load acting on the structure

is the vertical force applied to the top face (F). In a pin jointed structure, this force is evenly distributed among the four beams and can be expressed by:

$$P = \frac{F}{4\sin(\theta)}. \tag{1}$$

Here F is the vertical load on the unit cell, P is the resolved axial load in the beams, and $\theta = 45°$ is the angle between the beams and the plane normal to the loading direction (Fig. 3b). In the idealized pin jointed structure with no offset at the central node, the only resulting load on a beam is this axial load. In the actual structure, the fixed boundary condition on the lower face of the beam causes it to undergo a vertical bending following a displacement condition on the top face that is proportional to its axial deflection. A displacement equation that accurately predicts the actual beam deflection can be found using classical beam bending models [19], as can the moment (M_2) and shear force (Q). This shear force and moment play a minimal role in the final deformation, so we omit their derivation here.

In an ideal structure, the axial load and the bending moment are the only resultant forces that act on the beams. Any imperfection in the beams or misalignment between the beams will lead to an additional torsional moment that acts at the central node of the structure. It is reasonable to assume that this moment M is generated solely by a misalignment in the central node of the structure and can therefore be approximated by multiplying the horizontal component of the axial load in the beams by the sum of the offset of each of the beams:

$$M = \frac{P}{\tan(\theta)}\sum_{i=1}^{4} d_i. \tag{2}$$

This moment can then be taken and resolved into each of the beams as a bending moment and a torsional moment as

$$M_1 = M\cos(\theta) = \frac{P\cos^2(\theta)}{\sin(\theta)}\sum_{i=1}^{4} d_i, \tag{3}$$

$$T = M\sin(\theta) = P\cos(\theta)\sum_{i=1}^{4} d_i. \tag{4}$$

It is important to impose proper boundary conditions for the deformation in this direction of the beam. The lower end of the beam was assumed to be rigid. If the unit cell were perfect, the symmetry of the unit cell would force the upper node to remain in the center of the structure. The deformed structure shown in Figs. 4c and 5c demonstrates that the beams were able to pivot about the central node. While all of the beams in the structure provide some torsional resistance to buckling, due to the symmetry of the beam buckling, the effect is minimal. Therefore, the top node is assumed to have a pinned boundary condition, making the beam deflection governed by a fixed–pinned boundary condition. This is a critical consideration in calculating the overall strength of the structure.

Buckling response

Experimental and computational observations suggest that a buckling instability is the cause of the observed deflection of the beams. The complex loading and boundary conditions render a simple uniaxial buckling model incapable of characterizing the deformation of nanolattices observed here. We use a fundamental set of coupled differential equations, defined by [20], to characterize the deflection.

$$EI_y\frac{\mathrm{d}^4u}{\mathrm{d}x^4} + P\frac{\mathrm{d}^2u}{\mathrm{d}x^2} - M_1\frac{\mathrm{d}^2\phi}{\mathrm{d}z^2} = 0 \tag{5}$$

$$EI_z\frac{\mathrm{d}^4v}{\mathrm{d}x^4} + P\frac{\mathrm{d}^2v}{\mathrm{d}x^2} + M_2\frac{\mathrm{d}^2\phi}{\mathrm{d}z^2} = 0 \tag{6}$$

$$C_1\frac{\mathrm{d}^4\phi}{\mathrm{d}x^4} - \left(C - P\frac{I_o}{A}\right)\frac{\mathrm{d}^2\phi}{\mathrm{d}x^2} - M_1\frac{\mathrm{d}^2u}{\mathrm{d}z^2} + M_2\frac{\mathrm{d}^2v}{\mathrm{d}z^2} = 0 \tag{7}$$

Here u is the deflection of the beam in the z-direction, v is the deflection of the beam in the y-direction, and ϕ is the twist of the beam. P is the axial load in the beam, M_1 is the lateral bending moment and linearly dependent on P, M_2 is the vertical bending moment, and A is the area of the ellipse (Fig. 3c). I_y, I_z, and I_o are the second moments of area about the major and minor axis and the polar moment of inertia of the ellipse, respectively. C_1 is the warping constant of the beam, which can be taken to be zero for an elliptical beam, and C is the torsional constant. The equations for these variables in the context of a thick-walled hollow elliptical cylinder are as follows.

$$A = \pi(ab - (a-t)(b-t)) \tag{8}$$

$$I_y = \frac{\pi}{4}\left(ab^3 - (a-t)(b-t)^3\right) \tag{9}$$

$$I_z = \frac{\pi}{4}\left(a^3b - (a-t)^3(b-t)\right) \tag{10}$$

$$I_o = \frac{\pi}{4}\left[ab\left(a^2+b^2\right) - (a-t)(b-t)\left((a-t)^2+(b-t)^2\right)\right] \tag{11}$$

$$C = \pi G\left[\frac{a^3b^3}{a^2+b^2} - \frac{(a-t)^3(b-t)^3}{(a-t)^2+(b-t)^2}\right] \tag{12}$$

In these equations, a and b are the principal axes of the ellipse, as defined in previous sections. Based on these equations, the area of the beam is $A = 1.78 \times 10^{-13}$ m^2, the moment of inertia about the vertical axis is $I_y = 1.19 \times 10^{-27}$ m^4, the moment of inertia about the

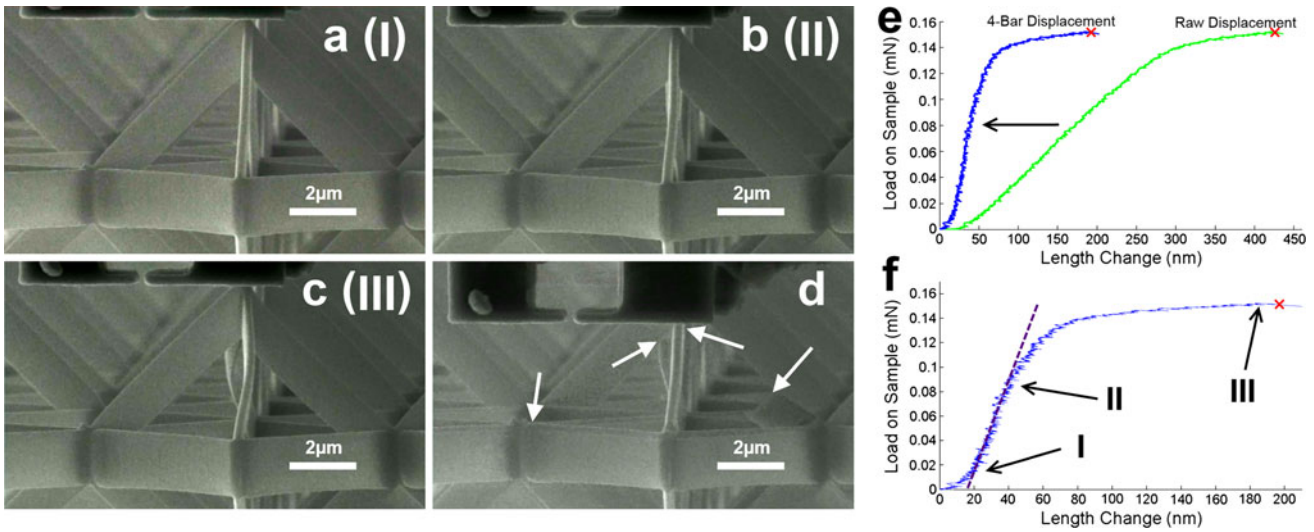

Fig. 4 Monotonic compression of unit cell. **a–c** SEM images captured during the monotonic compression experiment, showing the progressive buckling of the unit cell. These snapshots are correlated to positions *I*, *II*, and *III* in the load–displacement curve in **f**. **d** The *arrows* shown here point to local fracture points. It should be noted that the fracture positions closely match the stress concentrations seen in the FEM simulations (Fig. 6c). **e** Load–displacement data is corrected to only account for the deflection of the upper 4 bars of the unit cell. The *red x* indicates the point of failure. **f** Zoom in of the load–displacement plot showing the initial linear behavior and subsequent deviation from linearity (Color figure online)

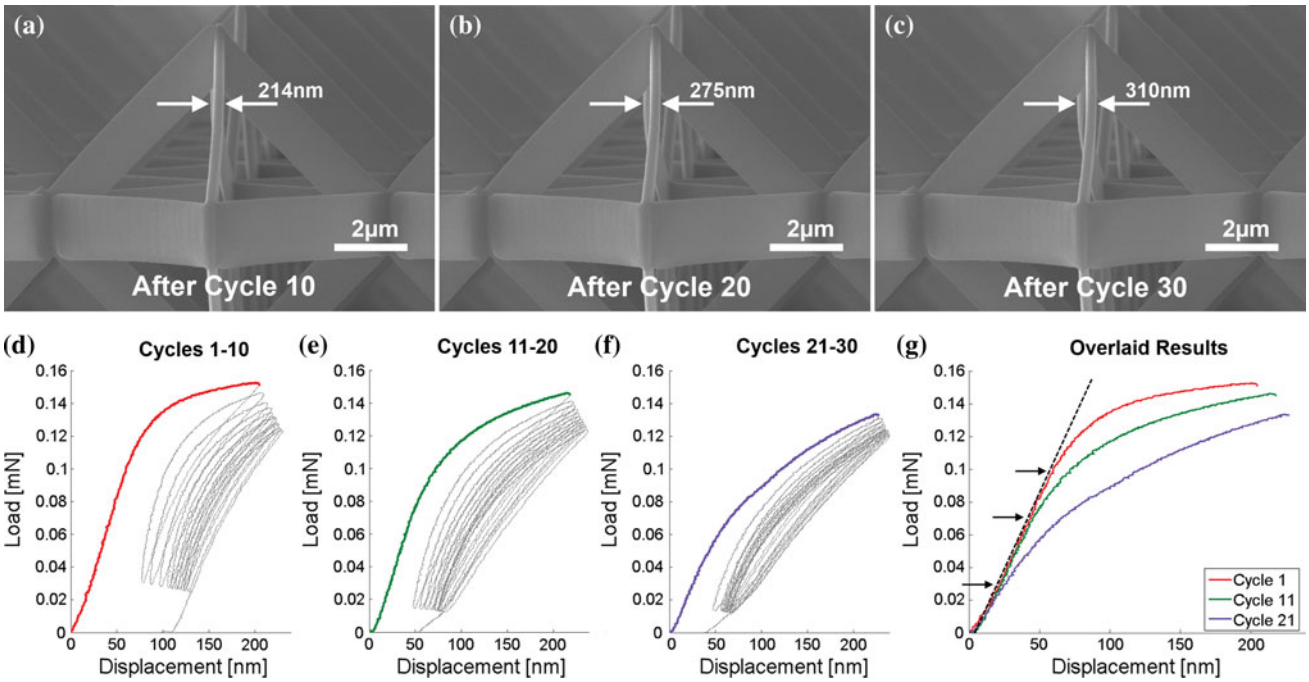

Fig. 5 Cyclic compression of unit cell. **a–c** Images showing progressive bowing of beams during cyclic compressive loading. The bowing gives rise to a weakened load displacement response, as shown in the graph in **g**. Each image corresponds to an additional ten cycles of unloading–reloading. **d–f** Three rounds of cyclic loading experiments that were performed on a single unit cell of the structure. **g** The weakened load displacement response of the first compression in each of the cyclic loading experiments. This *graph* is shown to demonstrate the progressively earlier onset of nonlinearity, a response which closely matches that of a pre-bent beam buckling (Color figure online)

horizontal axis is $I_z = 2.47 \times 10^{-26}$ m^4, and the polar moment of inertia is $I_o = 3.57 \times 10^{-26}$ m^4. The torsion constant was calculated to be $C = 1.73 \times 10^{-16}$ N m^2. The horizontal moment of inertia of the beam (I_z) is roughly one order of magnitude greater than the vertical moment of inertia (I_y), which suggests that buckling will

likely only occur in the horizontal direction. This simplifies the deflection equations from three sets of coupled ODEs to two equations of the form

$$EI_y \frac{d^4u}{dx^4} + P\frac{d^2u}{dx^2} - M_1\frac{d^2\phi}{dz^2} = 0 \quad (13)$$

$$\left(C - P\frac{I_o}{A}\right)\frac{d^2\phi}{dx^2} - M_1\frac{d^2u}{dz^2} = 0. \quad (14)$$

The fixed–pinned boundary condition of the beam for deflection in the z-direction leads to the following forms for the deflection and twisting equations of the beam:

$$u(x) = A_1(\sin(\kappa x) - \kappa x\cos(\kappa)) \quad (15)$$

$$\phi(x) = A_2(\sin(\kappa x) - \kappa x\cos(\kappa)). \quad (16)$$

Here $\kappa L = 4.493$, which is the first solution to the inequality $\kappa L = \tan(\kappa L)$ [18]. Inserting these equations into Eqs. 13 and 14 results in a matrix with the coefficients A_1 and A_2:

$$\begin{bmatrix} EI_y\kappa^2 - P & M_1 \\ M_1 & C - \frac{I_o}{A}P \end{bmatrix}\begin{bmatrix} A_1 \\ A_2 \end{bmatrix} = \boldsymbol{BA} = 0 \quad (17)$$

To obtain a non-trivial solution, the determinant of the $\boldsymbol{B}$ matrix must be zero.

$$\mathrm{Det}(\boldsymbol{B}) = \left(EI_y\kappa^2 - P\right)\left(C - \frac{I_o}{A}P\right) - M_1^2 = 0 \quad (18)$$

The only unknown variable in this equation is the load P, which means that it is a quadratic that is solvable both analytically and numerically. In the case of $M_1 = 0$, we obtain the classical Euler buckling and torsional buckling solutions for a beam as described in [20]. In the presence of an additional bending moment, buckling will occur at a lower load.

Full structure compression

The octahedral geometry of the nanolattice fabricated in this study is a bending-dominated structure, and it can be compared to the classical model for open-cell foams. It is therefore possible to approximate the strength and modulus of the nanolattice using classical Gibson–Ashby cellular mechanics relations derived for open-cell foams [7]. For a brittle, open-cell foam, the modulus and strength scale with the relative density of the structure, defined as $\bar{\rho} = \rho/\rho_s$, as

$$E \approx E_s\bar{\rho}^2 \quad (19)$$

$$\sigma_{cr} \approx 0.2\sigma_{fs}\bar{\rho}^{3/2}. \quad (20)$$

Here E_s is the Young's modulus of the constituent material. σ_{fs} is the modulus of rupture of the constituent material, which is defined as the maximum tensile stress achievable before failure. The relative density scaling relations for the strength and modulus arise because of the bending-dominated nature of the structure, and the coefficient of 0.2 for the strength relation is due to the fact that the nanolattice is composed of a brittle material. The relative density of the structure in this work was computed to be $\bar{\rho} = 0.0136$, which was found using a computer-aided design (CAD) of the structure, and is similar to the relative density of other ultra-light materials like aerogels [21].

Due to the fact that the structure is comprised of vertically oriented elliptical tubes, the resulting structure is inherently anisotropic in both strength and stiffness. Specifically, the anisotropy will lead to a higher strength and modulus in the vertical direction. Structural anisotropy has been quantified by Gibson and Ashby [7] for structures with elongated unit cells, but has not been quantified for structures with anisotropic beam elements.

Results

Compression of individual unit cells

Uniaxial compression tests

Individual unit cells were compressed by applying a vertical load to the top node of the structure at a constant displacement rate of 10 nm s^{-1} until failure at a load of 0.152 mN. Figure 4e shows that the final axial displacement of the structure was roughly 420 nm, which includes both the compression of the upper four beams and the deflection of the surrounding structure. This load–displacement data was subsequently corrected to only account for the vertical compression of the upper four beams (Fig. 4e), measured to be approximately 200 nm based on in situ SEM video frames. In the correction, it was assumed that the displacement of the surrounding structure remained in the linear elastic regime.

There was a notable deviation from linear behavior in the load–displacement data, as is indicated in (Fig. 4f). In situ video analysis confirmed that this deviation likely coincides with the initiation of lateral-torsional buckling in the struts (Fig. 4b, c). The final deformation of the structure was accommodated by lateral bending and twisting of the struts, until brittle failure at the midpoints of the beams and at the nodes (Fig. 4d).

Cyclic loading tests

A single unit cell was compressed in a set of cyclic loading experiments at a constant displacement rate of 10 nm s^{-1} to a total raw displacement of 350 nm and a subsequent unloading to 10 % of the maximum load in the cycle. The

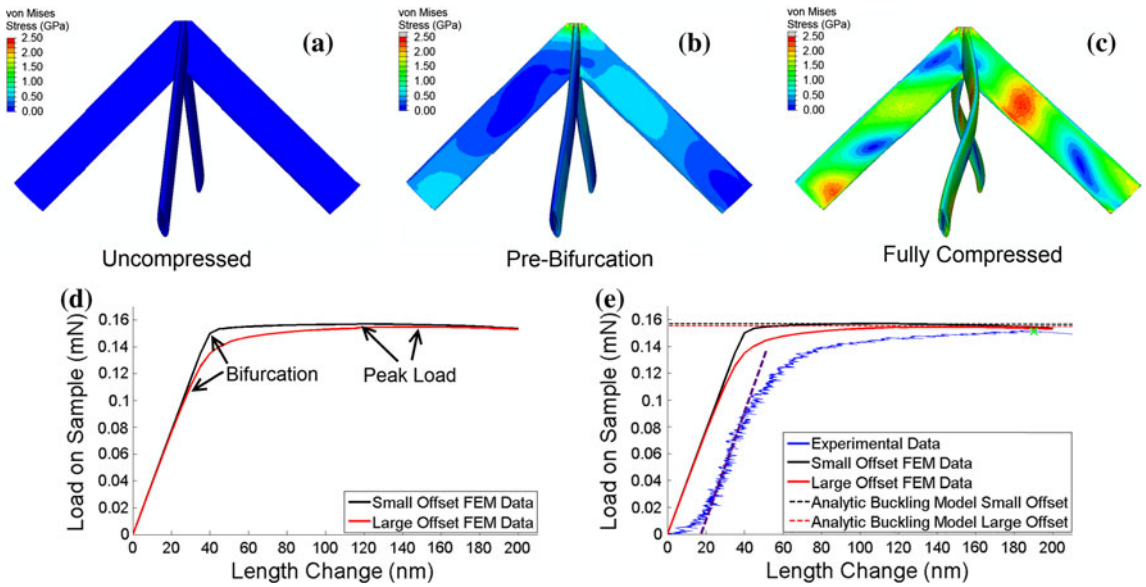

Fig. 6 Finite element analysis of upper unit cell. **a** Uncompressed FEM model of a 4-bar structure. **b** 4-bar structure under compression before the initiation of buckling. This corresponds to the bifurcation point in **e**. **c** Fully compressed 4-bar structure showing the full extent of deflection. This corresponds to the end of the FEM load displacement curve. **d** The load displacement response of the FEM simulations on the small and large-offset beams. **e** Fully overlaid unit cell compression results showing experimental, FEM, and analytic data. The superposition is intended to demonstrate the close agreement between the results of the three methods. The *green x* indicates the point of failure (Color figure online)

unit cell underwent three rounds of ten load–unload cycles (Fig. 5d–g). This data shown in these figures was corrected to account for the vertical deflection of the lower nodes of the structure in the same manner as for the monotonic compressions. The unit cell survived cyclic compression loading of up to 95 % of the maximum load prescribed in the uniaxial test without failure. A gradual decay in the maximum load reached during the compression of the unit cell was observed in each subsequent load–unload cycle (Fig. 5g). The large strain recovery seen during cyclic loading (Fig. 5d–f) implies that the deformation was primarily elastic, and that the observed hyperelasticity was likely a structural response and not a material response. Additionally, the decreased loading response seen in the initial loading for each of the three tests (Fig. 5g) closely matches the buckling response of a pre-bent beam [22]. This point is discussed in greater detail in section "Deformation of a single unit cell."

Finite element modeling

To explore the effect that the geometry of the unit cell has on the resulting deformation, a number of different beam models with varying degrees of offset in the central node of the structure were created and compressed using a nonlinear elastic FEM solver in ABAQUS. First, an ideal beam model with no offset in the central node of the structure was tested. The resulting deformation was linear and did not reproduce the lateral deflection seen in the experiments. Several beam models with systematically varying degrees of central offset were then created in an attempt to better match the actual geometry of the structure (Fig. 3c–e). In the deformation response of these offset FEM models, the beams first displayed a linear elastic behavior that continued up to a displacement of 30–40 nm and then rapidly began to twist and bend (Fig. 6), which very closely matched the behavior observed experimentally. Exploring a variety of beams with systematically varying degrees of offset in the central node of the structure revealed that any degree of offset qualitatively reproduced an identical bending and twisting response. The final deformed state of the structure and the final stresses in the beams were similar for the entire array of central offsets used, which ranged from one tube with a 20-nm offset to four tubes each with a 40-nm offset (Fig. 3).

The vertical reaction force, defined here as the sum of the forces on the nodes at the top face of the structure, was measured for different beam models. As the degree of offset in the central nodes became greater, it was observed that the onset of nonlinear behavior occurred at a lower load (Fig. 6d). The resulting load–displacement data for two structures, one with a 20-nm offset of a single beam (small-offset) and one with a 40-nm offset of all of the beams (large-offset), is presented alongside the experimental data (Fig. 6e). The critical load at which the bifurcation occurred was found to be $F = 0.152$ mN in the

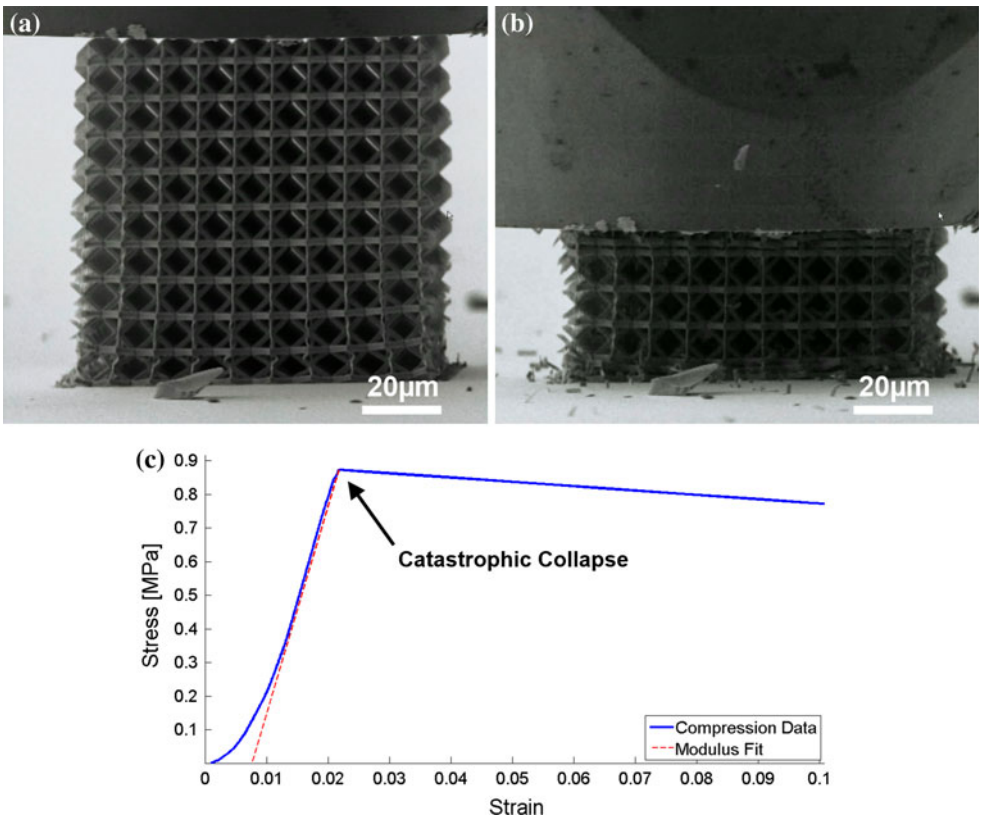

Fig. 7 Full structure monotonic compression. **a** Full structure at the beginning of a compression test. **b** Structure after the collapse point indicated in the *graph*. **c** Stress–strain data from the compression of the above structure (Color figure online)

small-offset beam and $F = 0.135$ mN for the large-offset beam. The peak load in the small-offset beam was $F_{max} = 0.157$ mN and $F_{max} = 0.154$ m for the large-offset beam.

Analytical model

A larger lateral offset of the beams from the central node of the structure generates a higher bending moment, which effectively lowers the force necessary to initiate buckling. In the ideal case where $M_1 = 0$, it was calculated that the minimum load required to buckle an individual strut is $P_{cr} = 55.5$ μN. When this calculation is performed using a moment $M_1 = 1.13 \times 10^{-7}$ Nm, which corresponds to the approximate moment induced during the compression of the large-offset structure, the critical load drops down to $P_{cr} = 55.0$ μN. Using Eq. 1, these loads are multiplied by $2\sqrt{2}$ to calculate the effective resolved load in the 4-bar setup of the compression of a unit cell. The resulting applied force F that is needed to buckle the struts in the full unit cell structure is 0.157 mN for a structure with no central moment, meaning no offset, and 0.155 mN for the beam with a central moment of M_1. These values are plotted along with the experimental results and the data from the FEM simulations (Fig. 6e).

Compression of the full structure

The full nanolattice was compressed inside an in situ microscope at a displacement rate of 250 nm s^{-1} until failure at a peak load of 7.50 mN and a displacement of 1.92 μm. The resulting load–displacement curve and images of the initial and final states of the structure are shown (Fig. 7). The initial linear loading of the structure was followed by a brittle catastrophic collapse at the peak stress. The post-deformed image of the structure (Fig. 6b) shows the six topmost unit cells were fully compressed to failure. A full collapse of the structure was prevented due to a limitation in the travel distance of the indenter. The stress and strain at failure were estimated to be $\sigma_y = 0.873$ MPa and $\varepsilon_y = 0.0218$ using a measured top surface area $A = 8588$ μm^2 and a height $h = 88.0$ μm. The elastic modulus, calculated to be $E = 61.8$ MPa, was found using the loading slope of the stress–strain data.

Gibson–Ashby model

Using a classical open-cell brittle cellular material model given by [7] with a constituent material modulus of $E_s = 98$ GPa and a modulus of rupture of $\sigma_{fs} = 1.75$ GPa

as obtained from finite element experiments, the structural stiffness and strength were calculated to be

$$E = E_s\bar{\rho}^2 = (98\,\text{GPa})(0.0137)^2 = 18.39\,\text{MPa}$$

$$\sigma_{cr} = 0.2\sigma_{fs}\bar{\rho}^{\frac{3}{2}} = 0.2(1.75\,\text{GPa})(0.0137)^2 = 0.559\,\text{MPa}.$$

The regular Gibson–Ashby model for the Young's modulus and modulus of rupture of the structure does not adequately predict the experimentally determined properties. The modulus is under-predicted by a factor of 3.35 and the strength is under-predicted by a factor of 1.56. This is primarily due to the anisotropy of the structure, a point that will be discussed further in the following sections. The order of magnitude of the modulus and strength predictions is correct, implying that the structure still approximately follows a Gibson and Ashby scaling, but a more detailed constitutive model is needed to account for the anisotropy effect of the tubes.

Discussion

Constituent material properties

Bulk titanium nitride is typically a brittle ceramic, whose failure is governed by microstructural flaws [23]. The tensile yield strength of 1.75 GPa obtained from FEM modeling in this work appears to be 1–2 orders of magnitude higher than values reported for typical bulk ceramics, which generally range from tens to hundreds of MPa [24]. We attribute the high tensile yield strength in the ALD-deposited TiN to the competition between internal (microstructural) heterogeneities like grain boundaries and constituent material defects. Nanocrystalline TiN is inherently brittle, and will fail via fracture at the location of the highest stress concentration within the material, such as a pore or a crack. For bulk materials, these flaws play a key role in the determination of the yield stress. A reduction in sample size is accompanied by a corresponding decrease in the maximum flaw size, which leads to a lower probability of finding a weak flaw. When the sample becomes sufficiently small, at some critical size the stress concentration at the weakest flaw may become comparable to the stress concentrations in the microstructure of the material, i.e., grain boundary triple junctions. Recent work by Gu, et al. reported that failure in nanocrystalline platinum nanostructures was not governed by the presence of external notches but was driven by microstructural heterogeneities [17, 25]. This transition coincides with a yield strength that is governed by grain boundary failure and represents a significant fraction of the theoretical material fracture strength, approximated to be between $E/2\pi$ and $E/30$ [26, 27]. The high yield strength of the samples in this experiment is discussed in greater detail in [17].

The Young's modulus of 98 GPa found in the experiments is on the lower end of the range of the reported values for bulk TiN [24, 28]. The most likely causes of the reduced Young's modulus are the porosity of ALD-deposited material and the grain size of 10–20 nm in the TiN films, the most critical of which being the porosity of the sample. The modulus of a material is highly dependent on density, and lower relative density materials can have considerably reduced Young's moduli [29]. The modulus has been shown to decrease linearly with relative density for a number of materials. For example, in work by Andrievski [28], it was shown that the modulus of TiN had a strong linear scaling with relative density, with a porosity of 20 % corresponding to an 80 % reduction in the modulus. It has been shown that atomic layer deposition (ALD) onto polymers may result in lower film densities because the gas-phase reactants can diffuse into the polymer [30]. While the porosity of our material was not thoroughly investigated, it is likely a major contributor to the observed reduction in modulus. The other important factor in the modulus reduction is the nanocrystalline microstructure of the TiN in this work, with the grains on the order of 10–20 nm (Fig. 2c). For materials with nanocrystalline grains, a larger volume fraction of the material is comprised of grain boundaries, which have been shown to be less dense than a regular crystal lattice, and therefore have a lower Young's modulus [29]. When the grain size of iron, copper, and palladium samples was reduced to 10–20 nm in [29], a decrease of up to 26 % in the Young's modulus was reported and explained through the increased volume fraction of grain boundaries. This combination of high porosity and nanometer-sized grains may explain the reduction in the modulus from a maximum of $\sim$490 GPa reported in literature for fully dense bulk TiN [28] to the 98-GPa found in this study.

Deformation of a single unit cell

There is a strong agreement between the experimental results and the FEM simulations, both qualitatively in the observed deflection (Figs. 4a–c, 6a–c) and quantitatively in the load–displacement data (Fig. 6e). The non-trivial amount of recovery in the cyclic experiments (Fig. 5d) suggests that the deformation was primarily elastic. Additionally, the TiN in the experiment was nanocrystalline, meaning that there are few mechanisms for plasticity [31]. Although there is some permanent deformation observed, it is minimal and only observed after many compression cycles at loads close to the failure limit. The close agreement between the experimental results and the FEM results indicate that the elastic model was able to sufficiently

replicate the behavior seen experimentally. The additional residual displacement seen in the cyclic loading of the structure can likely be attributed to cracking at the lower nodes and to the slight bowing of the beam (Fig. 5a–c).

We observe that the maximum load obtained in the FEM simulations of the small-offset and the large-offset structures closely matched the load obtained in the analytical buckling analysis. The initiation of buckling in the FEM model occurred at a lower load than the theoretical buckling load for both structures (Fig. 6e). The large-offset structure displayed a greater deviation from the theoretical buckling load than the small-offset one, which implies that the effect of the offset can be explained in the context of a structural imperfection. In a perfect beam, when the structure reaches the critical buckling load, there is a sudden jump to the buckled state that corresponds to a bifurcation in the load. Any imperfection in the beam, such as a bend, surface roughness, or waviness, facilitates a more gradual transition to the buckled state because the beam has been locally pre-bent, with larger imperfections leading to greater deviations from perfect buckling. This behavior is described in detail in [22], where the degree of deviation from the perfect beam buckling response is directly related to a parameter $k = a/r$. Here, a is the lateral offset of the bent beam from the perfect structure and r is the radius of gyration, defined as $r = \sqrt{I/A}$, where I is the second moment of area in the buckling direction and A is the cross-sectional area of the beam. This behavior was directly observed during the cyclic load response of the beams (Fig. 5g), and was replicated with the small and large-offset FEM models. The analytic buckling model does not account for any imperfections, which means it is predicting the critical load necessary to initiate buckling in a perfect beam and is not able to account for any imperfections.

The close agreement between the deflection behavior observed experimentally, the FEM modeling, and the analytic beam buckling approach strongly suggests that the observed deflection of the structure was due to a buckling instability. Equations 13 and 14 show lateral and torsional buckling are coupled due to the additional central moment in the structure. Therefore, any lateral buckling of the beam will couple with torsional buckling resulting in lateral-torsional buckling [32, 33], as was observed in both the experimental results and the FEM model.

The hysteresis observed in the cyclic load displacement data may be explained by accounting for the friction between the top surface of the structure and the indenter tip. The steep inclination of the beams means that friction will play a lesser effect on the onset of buckling because it does not act as directly in the direction of the buckling. The unbuckling response will still have a hysteresis, as demonstrated experimentally in [34, 35].

Full structure

Using the classical cellular solids models given by Gibson and Ashby [7], the modulus and yield stress of a 3D nanolattice was approximated. These laws had been derived analytically for an isotropic, open-cell material with solid walls, where a bending of the beams gives rise to high stress concentrations near the nodes of the structure. The nanolattice material, which is a bending-dominated structure with hollow thick-walled beams, has similar conditions to those used in the analytic derivation, and it is therefore reasonable that they would follow a similar, although not identical, scaling law. The biggest difference comes from the large anisotropy of the elliptical tubes, which have an aspect ratio of 4.5:1. This high aspect ratio gives the tubes a moment of inertia in the vertical direction that is roughly one order of magnitude higher than that in the horizontal direction. Because the analytic model for a bending-dominated structure assumes isotropic beam bending, it is insufficient to perfectly analyze the structure, although it still can be used to obtain a reasonable approximation.

The strength and modulus of the nanolattice are underestimated by the classical Gibson and Ashby scaling laws by a factor of 1.56 and 3.35 times, respectively. This discrepancy was expected given the anisotropy of the beams. The difference between the experimental and analytic results for the strength and modulus can be explained using anisotropy results that have been derived previously for anisotropic structures with elongated unit cells. It is shown in [7] that the degree of anisotropy in the modulus and strength can be quantified using an anisotropy ratio R, defined as the ratio between vertical and transverse dimensions of a unit cell. In these equations, the anisotropy in the modulus scales approximately with R^2, and the strength anisotropy scales approximately with R, meaning that the modulus is much more sensitive to the anisotropy than the strength. While the scaling equations used in [7] do not directly apply to anisotropic beam members, they do suggest that the discrepancy observed between the experimental and analytic results follows the correct trend. A more in depth derivation is needed to properly account for the anisotropy of the beams in an analytical model.

The failure mode of the 4-bar unit cell structure was elastic buckling followed by fracture near the midpoints of the beams, but this failure mode cannot be generalized to the entire structure, which experiences a more complex stress state. Additional failure modes might be activated as a result of bending and twisting actions of the beams. The experiments performed on the individual unit cells allows us to gain some insight into the possible failure mechanisms, and additional studies on the entire structure are necessary to fully understand the range of possible failure

modes. The results of these investigations are being prepared for a separate manuscript.

Conclusions

We have demonstrated the capability to fabricate, mechanically test, and accurately analyze the mechanical response of cellular architected materials with features ranging from nanometer to micron to millimeter length scales. Results indicate that the tensile yield strength of the constituent titanium nitride was 1.75 GPa, a value 1–2 orders of magnitude greater than that of the bulk material. Such improved strength likely stems from material size effects, whereby a reduction in the thickness of the walls to nanoscale dimensions allows for a higher constituent material strength and induces the emergence of damage resistance. Using a combination of computational and analytical methods, we were able to accurately predict the behavior and stresses observed in a single unit cell of the structure. Classical cellular solids scaling laws gave a reasonable first order approximation of the strength and stiffness of the full nanolattice structure, but more work is needed to properly account for the anisotropy of the beams comprising the structure.

Acknowledgements The authors gratefully acknowledge the financial support from the Dow-Resnick Innovation Fund at Caltech, the Office of Naval Research (Grant N000140910883) and the Army Research Office through the Institute for Collaborative Biotechnologies (ICB) at Caltech (ARO Award number UCSB.ICB4b). Part of this work was carried out at the Jet Propulsion Laboratory under a contract with NASA. The authors acknowledge critical support and infrastructure provided by the Kavli Nanoscience Institute at Caltech. The authors thank Dongchan Jang for his help with nanomechanical experiments. The authors also thank Frank Greer for his help in the ALD deposition of the TiN films.

References

1. Hutchens SB, Needleman A, Greer JR (2012) A microstructurally motivated description of the deformation of vertically aligned carbon nanotube structures. Appl Phys Lett 100:121910
2. Pathak S, Lim EJ, Abadi PPSS, Graham S, Cola BA, Greer JR (2012) Higher recovery and better energy dissipation at faster strain rates in carbon nanotube bundles: an in situ study. ACS Nano 6:2189–2197
3. Cao A, Dickrell PL, Sawyer WG, Ghasemi-Nejhad MN, Ajayan PM (2005) Super-compressible foamlike carbon nanotube films. Science 310:1307–1310
4. Schaedler TA, Jacobsen AJ, Torrents A, Sorensen AE, Lian J, Greer JR, Carter WB (2011) Ultralight metallic microlattices. Science 334:962–965
5. Torrents A, Schaedler TA, Jacobsen AJ, Carter WB, Valdevit L (2012) Characterization of nickel-based microlattice materials with structural hierarchy from the nanometer to the millimeter scale. Acta Mater 60:3511–3523
6. Sandhage KH, Dickerson MB, Huseman PM, Caranna MA, Clifton JD, Bull TA, Heibel TJ, Overton WR, Schoenwaelder ME (2002) Novel, bioclastic route to self-assembled, 3D, chemically tailored meso/nanostructures: shape-preserving reactive conversion of biosilica (diatom) microshells. Adv Mater 14:429–433
7. Gibson LJ, Ashby MF (1999) Cellular solids: structure and properties, 2nd edn. Cambridge University Press, Cambridge
8. Fleck NA, Deshpande VS, Ashby MF (2010) Micro-architectured materials: past, present and future. Proc R Soc A 466:2495–2516
9. Pellegrino S, Calladine CR (1986) Matrix analysis of statically and kinematically indeterminate frameworks. Int J Solids Struct 22:409–428
10. Hutchinson RG, Fleck NA (2006) The structural performance of the periodic truss. J Mech Phys Solids 54:756–782
11. Deshpande VS, Fleck NA, Ashby MF (2001) Effective properties of the octet-truss lattice material. J Mech Phys Solids 49:1747–1769
12. Tekoğlu C, Gibson LJ, Pardoen T, Onck PR (2011) Size effects in foams: experiments and modeling. Prog Mater Sci 56:109–138
13. Hamm CE, Merkel R, Springer O, Jurkojc P, Maier C, Prechtel K, Smetacek V (2003) Architecture and material properties of diatom shells provide effective mechanical protection. Nature 421:841–843
14. Luz GM, Mano JF (2009) Biomimetic design of materials and biomaterials inspired by the structure of nacre. Philos Trans R Soc A 367:1587–1605
15. Wang C, Huang Y, Zan Q, Guo H, Cai S (2000) Biomimetic structure design: a possible approach to change the brittleness of ceramics in nature. Mater Sci Eng C 11:9–12
16. Tetrault N, Freymann G, Deubel M, Hermatschweiler M, Perez-Willard F, John S, Wegener M, Ozin GA (2006) New route to three-dimensional photonic bandgap materials: silicon double inversion of polymer templates. Adv Mater 18:457–460
17. Jang D, Meza L, Greer F, Greer JR (2013) Fabrication and deformation of three-dimensional hollow ceramic nanostructures. Nat Mater 12:893–898
18. Kim JY, Greer JR (2009) Tensile and compressive behavior of gold and molybdenum single crystals at the nanoscale. Acta Mater 57:5245–5253
19. Timoshenko SP (1934) Theory of elasticity, 1st edn. McGraw-Hill Book Company, New York
20. Timoshenko SP, Gere JM (1961) Theory of elastic stability, 2nd edn. McGraw-Hill Book Company, New York
21. Akimov YK (2003) Field of application of aerogels (review). Instrum Exp Tech 46:287–299
22. Jones RM (2006) Buckling of bars plates and shells, 1st edn. Bull Ridge Publishing, Blacksburg
23. Kumar S, Wolfe DE, Haque MA (2011) Dislocation shielding and flaw tolerance in titanium nitride. Int J Plast 27:729–747
24. Shackelford JF, Alexander W (2000) Materials science and engineering handbook, 3rd edn. CRC Press Inc., Boca Raton
25. Gu XW, Wu Z, Zhang YW, Srolovitz DJ, Greer JR (2013) Flaw-driven failure in nanostructures. Nanoletters 13:5703–5709
26. Gao H, Ji B, Jager IL, Arzt E, Fratzl P (2003) Materials become insensitive to flaws at nanoscale: lessons from nature. Proc Natl Acad Sci 100:5597–5600
27. Meyers MA, Chawla KK (1998) Mechanical behavior of materials, 1st edn. Prentice-Hall Inc., Upper Saddle River
28. Andrievski R (1997) Physical-mechanical properties of nanostructured titanium nitride. Nanostruct Mater 9:607–610
29. Kim HS, Bush MB (1999) The effects of grain size and porosity on the elastic modulus of nanocrystalline materials. Nanostruct Mater 11:361–367
30. George SM (2010) Atomic layer deposition: an overview. Chem Rev 110:111–131
31. Sanders PG, Eastman JA, Weertman JR (1997) Elastic and tensile behavior of nanocrystalline copper and palladium. Acta Mater 45:4019–4025

32. Law K, Gardner L (2012) Lateral instability of elliptical hollow section beams. Eng Struct 37:152–166
33. Li C, Ru CQ, Mioduchowski A (2006) Torsion of the central pair microtubules in eukaryotic flagella due to bending-driven lateral buckling. Biochem Biophys Res Commun 351: 159–164
34. McCann RC and Suryanarayana PVR (1994) Experimental study of curvature and frictional effects on buckling. In: Offshore technology conference
35. Suryanarayana PVR, McCann RC (1995) An experimental study of buckling and post-buckling of laterally constrained rods. J Energy Res Technol 117:115–124